

Journal of the Royal Society Interface Focus

Aluminosilicate haloes preserve complex life ~800 million years ago

Ross P. Anderson^{1,2*}, Nicholas J. Tosca², Gianfelice Cinque³, Mark D. Frogley³, Ioannis Lekkas³, Austin Akey⁴, Gareth M. Hughes⁵, Kristin D. Bergmann⁶, Andrew H. Knoll⁷, Derek E.G. Briggs⁸

¹*All Souls College, University of Oxford, Oxford, OX1 4AL, UK*

²*Department of Earth Sciences, University of Oxford, Oxford, OX1 3AN, UK*

³*Diamond Light Source, Harwell Science and Innovation Campus, Didcot, OX11 0DE, UK*

⁴*Center for Nanoscale Systems, Harvard University, Cambridge, MA, 02138, USA*

⁵*Department of Materials, University of Oxford, Oxford, OX1 3PH, UK*

⁶*Department of Earth, Atmospheric, and Planetary Sciences, Massachusetts Institute of Technology, Cambridge, MA, 02139, USA*

⁷*Department of Organismic and Evolutionary Biology, Harvard University, Cambridge, MA, 02138, USA*

⁸*Department of Geology and Geophysics, Yale University, New Haven, CT, 06511, USA*

*Email: ross.anderson@all-souls.ox.ac.uk

1
2
3
4
5
6
7
8
9
10
11
12
13
14
15
16
17
18
19
20
21
22
23
24
25
26
27
28
29
30
31
32
33
34
35
36
37
38
39
40
41
42
43
44
45
46
47
48
49
50
51
52
53
54
55
56
57
58
59
60

ABSTRACT

Mudstone-hosted microfossils are a major component of the Proterozoic fossil record, particularly dominating the record of early eukaryotic life. Early organisms possessed no biomineralised parts to resist decay and controls on their fossilisation in mudstones are poorly understood. Consequently, the Proterozoic fossil record is compromised—we do not know whether changing temporal/spatial patterns of microfossil occurrences reflect evolution or the distribution of favourable fossilisation conditions. We investigated fossilisation within the ~1,000 Ma Lakhanda Group (Russia), and the ~800 Ma Svanbergfjellet and Wynniatt formations (Svalbard and Arctic Canada). Vertical sections of microfossils and surrounding matrices were extracted from thin sections by focused ion beam milling. Elemental mapping and synchrotron-based infrared microspectroscopy revealed that microfossils are surrounded by haloes rich in aluminium, likely hosted in kaolinite. Kaolinite has been implicated in Cambrian Burgess Shale-type (BST) fossilisation and is known to slow the growth of degraders. The Neoproterozoic mudstone microfossil record may be biased to tropical settings conducive to kaolinite formation. These deposits lack metazoan fossils even though they share fossilisation conditions with younger BST deposits that are capable of preserving non-mineralising metazoans. Thus metazoans, at least those typically preserved in BST deposits, were likely absent from sedimentary environments before ~800 Ma.

KEYWORDS

Proterozoic Eon, early eukaryotes, clay minerals, complex life, metazoan antiquity, taphonomy

INTRODUCTION

Due to a lack of organisms with readily fossilised hard parts, it has long been observed that the pre-Cambrian fossil record is impoverished compared to its Phanerozoic counterpart [1]. However, over the last ~70 years palaeontologists have discovered a number of exceptionally preserved assemblages of diverse microfossils in Proterozoic rocks [2, 3]. Three principal lithologies record microfossils: early diagenetic cherts and phosphates, and mudstones [4]. Evidence from the record of eukaryotic microfossils suggests that the mudstone record dominates—47 of 59 fossiliferous assemblages in a recent compilation are mudstone-hosted [4]. We know little of the taphonomic processes that operated in mudstones [5]. What factors promoted fossilisation? What determines which mudstones preserve non-biomineralised microfossils? Understanding taphonomy in Proterozoic mudstones is vital to our efforts to chart Proterozoic evolution. Furthermore, we need to understand whether there are temporal or spatial biases to the Proterozoic microfossil record. Patterns of microfossil diversity may represent real ecological patterns, but they could also represent spatial/temporal changes in the availability of environmental conditions conducive to fossilisation. Our inability to unravel these scenarios fundamentally compromises the use of mudstone-hosted microfossils to reveal Proterozoic evolutionary history.

Examples of soft-tissue fossilisation [6] in Phanerozoic mudstones provide a basis for taphonomic hypotheses that can be tested on Proterozoic deposits. Cambrian Burgess Shale-type (BST) deposits are the most studied, preserving early metazoans including diverse organisms that lacked mineralised skeletons [7]. A variety of factors have been proposed to influence BST fossilisation, including oxidant supply, sediment composition, the propensity of soft tissues for replication in authigenic minerals (e.g., pyrite, phosphate, and clay minerals), and cementation of

the overlying sediment [see 8 for review]. A role for clay minerals has been posited more recently: experiments have shown that the aluminium- and iron-rich clays kaolinite and berthierine, which are major constituents of a large proportion of Cambrian strata hosting BST fossils [9, 10], slow the growth of decay bacteria [11] and increase decay resistance through clay-organic matter interactions [12-18]. Evidence is also emerging that kaolinite, in particular, may attach to or precipitate on some tissues early in diagenesis, helping to conserve them by providing a protective coating and/or facilitating polymerisation [14, 19, 20]. Intriguingly, elements indicative of these clays (e.g., aluminium and iron) have also been reported adjacent to some Proterozoic fossils, but their host phases are difficult to constrain [21-23]. Do aluminium- and/or iron-rich clay minerals promote fossilisation in Proterozoic strata? Do they promote fossilisation not only of metazoans but of other phylogenetic groups such as eukaryotic algae, or even cyanobacteria, which have diverse biopolymer compositions?

We investigated the taphonomy of microfossils (both probable eukaryotes and cyanobacteria—table 1) from three exceptional Tonian (1,000–717 Ma) deposits: the ~1,000 Ma Lakhanda Group (Russia) [24, 25], and the ~800 Ma Svanbergfjellet (Svalbard) [26] and Wynniatt (Canada) formations [27]. These assemblages include some of the best preserved and most diverse pre-Ediacaran fossils, and often include microfossils that are more fragile than the decay-resistant spheroidal acritarchs commonly recovered from Proterozoic strata [2, 4]. More fragile forms include relatively large (up to mm-scale) multicellular morphologies and those that possess intricate spines or processes [7, 24-27]. For example, microfossils from the Svanbergfjellet Formation may represent some of the oldest examples of multicellular eukaryotic green algae (chlorophytes) [26, 28]. We used a novel combination of microanalytical techniques to probe sediment mineralogy immediately adjacent to microfossil cell walls. These data

88 illuminate the role of clay minerals in Proterozoic taphonomy, allowing comparisons to BST
89 fossilisation.

91 MATERIALS AND METHODS

92 Microfossils were identified in thin sections cut sub-parallel to sedimentary laminae that
93 were obtained for previous studies (as in BST fossilisation [7], fossils are compressed into two
94 dimensions parallel to laminae). Thin section number, university collection, and England Finder
95 coordinates are given in table 1 for each microfossil/population studied. Thin-sections from
96 Harvard University are deposited in the Paleobotanical Collections of the Harvard University
97 Herbaria, while the sections from the University of Cambridge are in the collections of N.
98 Butterfield. A filamentous microfossil (?sheathed cyanobacterium), *Siphonophycus*, was
99 examined from the Lakhandia Group, whereas three microfossils were analysed from the
100 Svanbergfjellet Formation: the chlorophyte *Proterocladus major*, the acanthomorphic acritarch
101 (?eukaryote) *Germinosphaera fibrilla*, and an unidentified fragment of a larger microfossil
102 (?eukaryote). A monostromatic population of spheroids, possibly *Ostiana* (?cyanobacterium) or
103 the ?chlorophyte *Palaeastrum* (we refer to this population as ?*Ostiana*) and another
104 *Siphonophycus* specimen were analysed from the Wynniatt Formation. For details on
105 phylogenetic assignments, see table 1. The microfossils from each deposit were derived from
106 single rock samples, one per deposit (Lakhandia, LK62, Cambridge; Svanbergfjellet, 86-G-62,
107 Harvard; Wynniatt, 88-KL-131, Cambridge). Vertical sections (~30 µm x 10 µm x 1 µm) of
108 microfossils and adjoining matrix were extracted perpendicular (or sub-perpendicular) to
109 sedimentary laminae from the thin sections using focussed ion beam (FIB) milling at the Harvard
110 Center for Nanoscale Systems (CNS) and attached to copper transmission electron microscopy

111 (TEM) grids. Milling was performed on a FEI Helios 660 Dual-Beam FIB/SEM (scanning
112 electron microscope), equipped with an Autoprobe 400 micromanipulator.

113 Vertical sections were imaged using the SEM on the FEI Helios 660 at CNS and also on
114 a Carl Zeiss Merlin SEM equipped with an Oxford Instruments X-Max^N 150mm² X-ray detector
115 at the University of Oxford Department of Materials (ODM). Energy dispersive X-ray
116 spectroscopy (EDS) at ODM was used to map elemental distributions across vertical sections for
117 all samples except *Germinosphaera* (which was destroyed in sample manipulation before maps
118 could be generated). In order to reduce sampling volume (thereby increasing spatial resolution)
119 and reduce charging effects, EDS was carried out at voltages below 10 kV, with higher energy
120 analysis to confirm the identify of elements when required (see Supplementary Material table S1
121 for configurations). Maps were processed using AZtec v3.3 and the TruMap function.
122 Synchrotron-based Fourier Transform Infrared (FTIR) microspectroscopy at the MIRIAM
123 beamline of Diamond Light Source was used to identify the mineral hosts of elemental variations
124 in all vertical sections. The beamline is coupled to a Bruker Vertex 80V FTIR spectrometer and
125 Hyperion 3000 microscope equipped with a 50 µm, LN₂ cooled, midband MCT detector. 256
126 scans were coadded at 4 cm⁻¹ spectral resolution per point. The infrared focal spot was confined
127 to a diffraction limited area using slits of effective aperture 3 x 3 µm at the sample, via x36
128 optics in transmission geometry with numerical aperture (NA) = 0.5. The sample was mapped
129 across this aperture with step size 1 µm, oversampling with respect to the aperture size. In these
130 conditions, the resulting spatial resolution is expected to be diffraction limited and wavelength
131 (λ) dependent, approximately at the Abbe resolution limit = $\lambda / 2NA = \lambda$ (at NA 0.5). The spatial
132 resolution is about 2.8 µm for the M-OH spectral region of interest.

Finally, powder X-ray diffraction (XRD) was performed on each rock sample using a PANalytical Empyrean diffractometer at the Oxford Department of Earth Sciences, employing a Co K α source and a PIXcel-1D detector. A substitute for the Svanbergfjellet sample, from the same locality/stratigraphic horizon, was obtained from Cambridge collections (sample 99-L-15) as no 86-G-62 material remains. Mineral identifications were confirmed using the ICDD (International Centre for Diffraction Data) Powder Diffraction File-4+ database (<http://www.icdd.com/products/pdf4.htm>) and the reference intensity ratio method [29]. Clay mineral species were distinguished by weak but diagnostic peaks commonly manifested as a composite reflection from 060 and/or 33-1 [30].

RESULTS

SEM imaging of the vertical sections revealed the cross-sectional structure of the microfossils (Fig. 1), which vary in thickness. The Svanbergfjellet microfossil *Proterocladus* is only tens of nm thick and hardly perceptible, while the Lakhanda *Siphonophycus* specimen and both the *Germinosphaera* specimen and the unidentified microfossil fragment from Svanbergfjellet are up to ~ 0.5 μm thick. All specimens from the Wynniatt Formation are intermediate in thickness (~ 0.2 – 0.4 μm). In some cases, microfossil walls have split and infilled with matrix, as in some of the Wynniatt *Ostiana* individuals, but the majority are intact. The Wynniatt *Ostiana* cluster is evident on two sedimentary laminae in the sample and thus may represent multiple colonies or one colony that has been infiltrated by sediment during deposition (Fig. 1). The *Siphonophycus* specimen from Lakhanda may be split into two or represents two superimposed filaments (Fig. 1). SEM images confirmed that microfossils are compressed sub-parallel to sedimentary laminae. The lithologies of the samples are similar, with most sediment

156 grains $\ll 1\ \mu\text{m}$ and only sparse grains $\sim 1\ \mu\text{m}$, around which microfossils may be deflected: e.g.,
157 the vertical section of the Lakhanda *Siphonophycus* (Fig. 1). Larger grains are normally rounded,
158 although some oblong sub-angular grains, which can reach $>5\ \mu\text{m}$ in maximum dimension (Fig.
159 1) with long axes parallel to sedimentary laminae, are associated with the Svanbergfjellet
160 microfossils.

161 EDS analysis revealed that the microfossils are composed of carbon (Fig. 1), although the
162 result was ambiguous for the Svanbergfjellet *Proterocladus* specimen, probably reflecting its
163 very thin cross-section and the relatively large volume producing X-rays which, even at 5–10
164 kV, can have a masking effect on local elemental enrichments. The Lakhanda *Siphonophycus*
165 specimen and the Wynniatt ?*Ostiana* specimens are enriched in sulphur. The sediment
166 surrounding all the microfossils is largely similar (see Supplementary Material, Fig. S2),
167 dominated by silicon and oxygen with minor aluminium, carbon, chlorine, iron, magnesium,
168 nitrogen, phosphorous, potassium, sodium, and sulphur, reflecting a siliciclastic matrix with
169 contributions from both organic matter and diagenetic minerals. Calcium is also present but
170 sparsely distributed, likely reflecting a minor admixture of carbonate minerals. Larger rounded
171 quartz grains are present (identified by a dominantly silicon and oxygen composition). Larger
172 sub-angular grains in Svanbergfjellet vertical sections are enriched in magnesium and iron,
173 indicative of chlorite.

174 Aluminium is generally enriched adjacent to microfossil carbon compared to the matrix,
175 often forming a halo (Fig. 1). Aluminium haloes with a thickness $<3\ \mu\text{m}$ are particularly apparent
176 surrounding the Svanbergfjellet unidentified microfossil fragment and the Lakhanda
177 *Siphonophycus* specimen. None of the Wynniatt vertical sections shows a contiguous halo, but
178 there are discontinuous aluminium enrichments adjacent to microfossils. The only vertical

section for which aluminium enrichments adjacent to microfossils were not identified unambiguously is that of the Svanbergfjellet *Proterocladus* specimen; however, as noted regarding its carbon composition, this may be due to its thin cross-section and EDS masking effects.

SEM imaging provides evidence that the aluminium enrichments occur in platy materials, presumably clays. SEM of the Wynniatt *Siphonophycus* vertical section shows a halo of platy material, parallel to sedimentary laminae, extending $<0.5\ \mu\text{m}$ around the microfossil (Fig. 2). A layer of matrix characterised by a lack of the larger grains or pseudo-hexagonal crystals that are common elsewhere (possibly muscovite) extends $<1\ \mu\text{m}$ beyond this layer. Coarser crystals often display planar interlocking boundaries, suggesting a phase of overgrowth after physical deposition. These observations indicate differential chemistry and mineralogy adjacent to the microfossil compared to that of the matrix. The finely crystalline and platy nature of the material hosting the aluminium enrichments identified by EDS suggests that aluminium may be bound largely in a clay mineral structure.

Synchrotron-based FTIR microspectroscopy confirmed that the most likely clay mineral host of these aluminium enrichments is kaolinite and its metamorphic products. Kaolinite can be identified using FTIR by a series of three M-OH bands at ~ 3620 , ~ 3652 , and $\sim 3694\ \text{cm}^{-1}$ [31]. For randomly oriented powders, the ~ 3620 and $\sim 3694\ \text{cm}^{-1}$ bands are more intense than the $\sim 3672\ \text{cm}^{-1}$ band; their frequencies are also sufficiently distinct from illite-group and chlorite-group minerals to allow unambiguous identification of kaolinite. FTIR microspectra from all Lakhanda and Svanbergfjellet vertical sections clearly differentiated these bands (Fig. 3). Vertical sections of the Wynniatt Formation fossils showed a broad M-OH band between ~ 3500 and $\sim 3700\ \text{cm}^{-1}$, with no observable kaolinite bands (Fig. 3). This likely reflects a dominance of

1
2
3 202 illite/muscovite in Wynniatt clay mineralogy [31]. Any kaolinite, if present, is diluted beyond the
4
5 203 detection limit in FTIR microspectra. Mild contact metamorphism of Wynniatt strata [32] may
6
7 204 have transformed kaolinite to illite/muscovite [33]. Microfossil carbon is not recorded in our
8
9 205 FTIR microspectra. Other Proterozoic microfossils are known to produce FTIR spectra indicative
10
11 206 of their carbon composition [34]. Its absence in our analysis likely reflects a drowning of any
12
13 207 organic signature given the limited amount of microfossil material compared to the mineral
14
15 208 matrix.

16
17
18
19 209 The total area under each band provides a proxy for the distribution of minerals. When
20
21 210 mapped across the vertical sections the areas under the $\sim 3694\text{ cm}^{-1}$ band and the entire M-OH
22
23 211 region show some variation between specimens (Fig. 4) but cannot be fully matched to the EDS
24
25 212 maps (Fig. 1, S2). In the Lakhanda *Siphonophycus* and Svanbergfjellet vertical sections both
26
27 213 FTIR bands are weaker on and around the microfossils, a contrast that is especially evident near
28
29 214 hotspots (red) where the bands are locally strong. This is indicative of a lack of OH within
30
31 215 microfossils at the $\sim 2.8\text{ }\mu\text{m}$ resolution of the FTIR map, rather than a lack of OH groups around
32
33 216 microfossils. In the Lakhanda *Siphonophycus* vertical section the region where OH bands are
34
35 217 weaker extends down vertically, perhaps corresponding to the larger quartz grain below the fossil
36
37 218 (Fig. S2). The source of the FTIR band hotspots is not evident in light microscopy or EDS
38
39 219 images (Fig. 1, S2), but overall we can conclude that kaolinite is present across the bulk of the
40
41 220 mineral phase of the four FTIR maps of the vertical sections in Fig. 4. The large black region on
42
43 221 the left side of the Lakhanda *Siphonophycus* FTIR maps is where the band strength is high and
44
45 222 saturated with respect to the colour scale in the image (>4.6 or >13 for the 3694 cm^{-1} and full M-
46
47 223 OH band respectively). This apparent increase in band strength may include optical effects of the
48
49 224 interaction between the infrared beam and the metallic weld close ($<5\text{ }\mu\text{m}$) to the attachment of
50
51
52
53
54
55
56
57
58
59
60

the sample to the TEM grid. The ratio of the $\sim 3694\text{ cm}^{-1}$ band to the entire M-OH region reflects the distribution of kaolinite with respect to total illite [31]. At the $\sim 2.8\text{ }\mu\text{m}$ spatial resolution available, a fairly constant abundance of kaolinite, with respect to total illite, across each vertical section is implied by the similar ratios, with no clear correspondence to the microfossils. The black zig-zag patterns along the edges of the vertical section are artefacts resulting from optical scattering from the vertical section. These biomineralogical data from synchrotron-based FTIR microspectroscopy confirm that kaolinite and/or its metamorphic products are present in all vertical sections. Although the FTIR maps do not fully resolve the distribution of minerals with the necessary spatial resolution, in concert with EDS maps they provide a compelling case for kaolinite enrichment adjacent to microfossils.

Further confirmation that kaolinite represents a component of the fossiliferous rocks is evident in bulk powder XRD analyses of hand samples from each locality (table 2), although these do not sample individual laminae. All samples are dominated by muscovite (34–74%, mean = 57.7, std. dev. = 21, n=3) and quartz (26–58%, mean = 37, std. dev. = 18.2, n=3); the Svanbergfjellet sample contains minor chlorite (7%) in addition. The reference intensity ratio method detected kaolinite (8%) only in the Lakhanda sample. However, weak but diagnostic peaks manifested as a composite reflection from 060 and/or 33-1 showed that kaolinite is also present in the Svanbergfjellet sample. Relative abundance of clay species can be obtained as a linear function of the area underlying these peaks [30]. This method shows that kaolinite represents 30.7% of total clay (glaucinite + illite type 1 + illite type 2 + kaolinite) in the Svanbergfjellet sample, and 66.2% in the Lakhanda sample. The high kaolinite content of the Lakhanda sample is consistent with mineralogical studies of these strata [35]. The absence of kaolinite from powder XRD and the high illite content (90%) of the Wynniatt sample is

1
2
3
4
5
6
7
8
9
10
11
12
13
14
15
16
17
18
19
20
21
22
23
24
25
26
27
28
29
30
31
32
33
34
35
36
37
38
39
40
41
42
43
44
45
46
47
48
49
50
51
52
53
54
55
56
57
58
59
60

consistent with the broad M-OH band in the FTIR data, perhaps reflecting complete transformation of any precursor kaolinite to illite/muscovite during contact metamorphism [32]. 060 and/or 33-1 composite reflections suggest that glauconite (10%) is also present in the Wynniatt sample.

DISCUSSION

Kaolinite and Proterozoic fossilisation

The identification of aluminosilicate haloes surrounding microfossils, hosted in kaolinite and its metamorphic products illite/muscovite, prompts comparisons to Cambrian BST fossilisation. Strata with BST fossilisation globally are enriched in berthierine (a diagenetic product of kaolinite when iron is present) [9, 10]. Recently it has also been observed that metazoan fossils from the Burgess Shale at the Walcott Quarry (Canada) are themselves enriched in kaolinite compared to their surrounding mudstone matrix [19, 20]. The kaolinite enrichment on Burgess Shale fossils is attributed to bonding between the fossil organic matter and the mineral during organism decay, which is inferred to have slowed or arrested subsequent transformation of fossil-associated kaolinite to other minerals during greenschist facies metamorphism [20, 36]. This interpretation implies that local decreases in pH induced by decay [37] result in positively charged carcass organic matter, facilitating bonding with negatively charged edge sites on kaolinite [e.g., 38, 39, 40]. These edge sites, which account for 10–20% of the surface area of the mineral [39], are known to be relatively acidic, increasing the likelihood that they would persist in a negatively charged state at relatively low pH, maximising the probability of binding to organic matter [41, 42]. It is unclear whether kaolinite attached to fossil organic matter was from the sediment, or whether it precipitated *in situ*. It has been argued that

the chemical properties of kaolinite were a significant factor in the fossilisation of Burgess Shale metazoans [19, 20]. Kaolinite is known to promote polymerisation and adsorption of a variety of organic molecules [38, 39, 43], and to trigger kerogen maturation upon pyrolysis [44]. It can stabilise pre-existing organic cross-links via the donation of electrons, reducing double bonds [45], as well as inhibit the growth of bacteria that promote decay [11]. Experimental studies have shown that kaolinite-organic interactions often promote the conservation of morphology in decaying metazoan tissues [12-18].

The aluminosilicate haloes surrounding the microfossils studied here suggest that kaolinite attachment and/or *in situ* precipitation onto microbial cell-walls or enclosing sheaths, via a similar process to BST fossilisation, was a significant factor in the preservation of microfossils in Proterozoic mudstones. These data add to recent studies that report concentrations of elements indicative of clays (e.g., aluminium and iron) adjacent to other Proterozoic fossils [21-23]. The organisms studied here likely represent a variety of evolutionary clades, including eukaryotic chlorophyte algae and cyanobacteria [24-28]. The cell walls and extracellular sheaths of these organisms were composed of different biomolecules (table 1) than those of the metazoans preserved in BST deposits, with variable resistance to decay [46, 47]. Cyanobacteria cells are commonly enclosed by sheaths composed of chemically distinct carbohydrate fibrils which are relatively resistant to decay [48]—in the case of *Siphonophycus*, for example. *Ostiana*, on the other hand, may not possess a sheath; the cell walls likely comprised lipids and proteins [49]. Chlorophytes are dominated by carbohydrates, including cellulose, which make up the cell walls. And acanthomorphic acritarchs, such as *Germinosphaera*, are commonly characterised by highly resistant walls of aliphatic composition similar to sporopollenin or algaenan [50]. In contrast, metazoans, like those represented in BST

1
2
3 294 deposits, are composed of a range of biomolecules including proteins, carbohydrates and lipids,
4
5 295 although sclerotised and cuticularised tissues are preferentially preserved [51]. The similarity of
6
7 296 kaolinite enrichments in fossils representing these different clades suggests that this type of
8
9
10 297 fossilisation is not biopolymer specific. Nor is it morphology dependent—the fossils studied here
11
12 298 range in morphology from filaments and spheroids, to multicellular remains, and in the case of
13
14 299 Burgess Shale fossils, macroscopic forms. Indeed, numerous studies have already shown that
15
16 300 clay minerals commonly attach to the organics of microbial organisms such as cyanobacteria in
17
18 301 natural and experimental systems [52-57]. The enrichments of kaolinite adjacent to microfossil
19
20 302 cell walls argues not only for a role for kaolinite in fossilisation but, through organism-mineral
21
22 303 interactions, a role for incipient microfossils in facilitating kaolinite enrichment in the first place.
23
24
25 304 A similar process has also been used as an explanation for silica enrichments surrounding
26
27 305 microfossils [58].
28
29
30
31 306

32
33 307 Biases of the Proterozoic shale-hosted microfossil record
34

35 308 Identifying a taphonomic role for kaolinite in Proterozoic mudstones, the dominant
36
37 309 lithology for early microfossils [4], indicates that the Proterozoic mudstone-hosted fossil record
38
39 310 may be biased to environmental settings that were rich in kaolinite or hosted conditions
40
41 311 conducive to its formation, giving us pause for thought when considering temporal/spatial
42
43 312 patterns in the Proterozoic microfossil record. Kaolinite today is primarily sourced from tropical
44
45 313 weathering regimes where drainage is high and soil pH low [33]. Palaeogeographic
46
47 314 reconstructions suggest that each of the studied deposits (Lakhanda Group – Siberia,
48
49 315 Svanbergfjellet Formation – East Svalbard, and Wynniatt Formation – Laurentia) formed in
50
51 316 tropical to mid palaeolatitudes [59], consistent with this interpretation. Moreover, reconstruction
52
53
54
55
56
57
58
59
60

of seawater pH through geologic time suggests that Neoproterozoic oceans were characterised by lower pH than their modern counterparts [60]. Such a palaeoenvironmental bias to fossilisation is likely to be more acute for organisms where preservation of delicate morphology is required. The three assemblages studied include rarely preserved morphologies that were presumably more fragile (e.g., multi-celled, slender spines/processes) than those from other Proterozoic localities with microfossils [24-27]. It is not clear from our work whether the presence of kaolinite in the local environment is sufficient or kaolinite is required at a specific concentration.

Implications for our understanding of the antiquity of metazoans

Our results have specific implications for understanding the emergence of metazoan life. There is a disconnect between molecular clock estimates for the antiquity of metazoans and their earliest body fossils. A recent molecular analysis placed the last common ancestor of extant metazoans at 833–650 Ma [61], yet unambiguous body fossil evidence extends only as far as ~580 Ma [e.g., 62]. Where are the missing pre-580 Ma metazoan fossils? Can the gap be explained by taphonomic bias [63]? BST fossilisation provides an unusually comprehensive picture of Cambrian metazoan diversity [61, 64-66]; even microscopic metazoans are represented [67, 68]. The demonstration that some Neoproterozoic mudstones share taphonomic pathways with BST deposits identifies at least three Tonian targets for early metazoan fossils. However, the microfossils in these assemblages represent microbial eukaryotes and bacteria [2, 24-28, 69-71]. Some large morphologically complex microfossils in Ediacaran mudstones have been interpreted as egg and/or diapause cysts of metazoans [72] and a similar interpretation has been advanced for a population of Tonian fossils [73], but other interpretations have been proposed [74]. Macroscopic fossils, e.g., *Chuaria* and *Tawuia*, occur in two of the deposits

1
2
3 340 (Svanbergfjellet and Wynniatt) [24-27] and, although recent evidence suggests that some of
4
5 341 these may be multicellular, there is no evidence that they represent metazoans [75]. The lack of
6
7 342 metazoan fossils in these deposits despite BST conditions conducive to their fossilisation, may
8
9
10 343 indicate that metazoans had not evolved by ~800 Ma. If so, this provides a soft maximum age (a
11
12 344 maximum age based on the probability that fossils of this age are not metazoans) for their
13
14 345 appearance, as suggested previously [67] and employed in some molecular clocks [64] but
15
16
17 346 without consideration of taphonomy. It could be argued that, even though metazoans are not a
18
19 347 component of the three assemblages that we investigated, they could be present in others of
20
21 348 similar age, or that small early metazoans are not preserved even by BST fossilisation.
22
23
24 349 Nonetheless this soft maximum age can now be applied with greater confidence.
25

26 350

27
28 351 Clay mineral-organic interactions and the search for fossils on Mars
29

30
31 352 Our results may also be relevant to the search for fossilised life on Mars [76]. A variety
32
33 353 of clay minerals have been identified on the basis of orbital infrared spectroscopy, including
34
35 354 illite, kaolinite, smectites, chlorites, and serpentine minerals [77-79]. Clay minerals have been
36
37 355 identified in crustal rocks that may encompass a wide range of palaeoenvironmental conditions.
38
39 356 These deposits have been variably interpreted as *in situ* weathering profiles, fine-grained clastic
40
41
42 357 sediments, and hydrothermally altered crust [77-79]. Our data suggest that specific interactions
43
44 358 between kaolinite mineral surfaces and solution may have facilitated the polymerisation of
45
46
47 359 organic molecules – a key step in promoting fossilisation. These reactions, though, are dependent
48
49 360 on the pH of the solution relative to the acidity of clay edge sites. It is reasonable to assume that
50
51 361 these same principles apply to the early Martian surface; in suitable chemical conditions,
52
53
54 362 kaolinite may have served a similar taphonomic role to that envisaged for samples described
55
56
57
58
59
60

here. However, available data indicate that clay-rich deposits on early Mars experienced a much broader range in pore/bottom water pH, variable contact times with liquid water, and large fluctuations in ionic strength [79, 80]. Thus, taphonomically favourable clay mineral assemblages on Mars are best diagnosed in light of depositional and diagenetic constraints on fluid chemistry and a mechanistic consideration of clay mineral-organic interactions.

CONCLUSIONS

An understanding of taphonomy is critical to the interpretation of morphology and the environmental/temporal ranges of fossil taxa, and is particularly important for Proterozoic palaeobiology where biomineralised tissues are absent. Kaolinite or its metamorphic equivalents are associated with all microfossils in the three Tonian deposits we studied, despite their phylogenetic, compositional, and stratigraphic diversity. Our search for new microfossils, particularly fragile metazoans, in Proterozoic strata should focus on sites where kaolinite is likely to be present. These search criteria may also be valid when exploring other planets, such as Mars [76], for evidence of past life. Further studies should expand this investigation to a wider variety of Proterozoic fossiliferous mudstones, such as those of the Ediacaran Doushantuo Formation which do not contain complex metazoans [81], in order to determine the prevalence of appropriate taphonomic conditions across time and palaeoenvironments.

AUTHOR CONTRIBUTIONS

RPA, NJT, KDB, and DEGB designed the research. AHK provided fossils. AA prepared vertical sections. RPA and GMH analysed vertical sections using SEM and EDS. RPA, GC, MDF, and IL analysed vertical sections using synchrotron-based FTIR microspectroscopy. RPA and NJT

1
2
3
4
5
6
7
8
9
10
11
12
13
14
15
16
17
18
19
20
21
22
23
24
25
26
27
28
29
30
31
32
33
34
35
36
37
38
39
40
41
42
43
44
45
46
47
48
49
50
51
52
53
54
55
56
57
58
59
60

analysed fossiliferous rocks using XRD. RPA wrote the manuscript with discussion and input from all authors.

ACKNOWLEDGEMENTS

We are grateful to N. Butterfield for access to fossils, valuable discussion, and comments on a draft of this paper. RPA thanks the organisers of the Royal Society Discussion Meeting for the invitation to present at the meeting, in addition to P. Donoghue for valuable discussion and H. Bechtel, E. Clark, K. Clayton, B. Johnson, W. Samela, and R. Tostevin for assistance with sample preparation and data collection. Diamond Light Source is acknowledged for beamtime SM15975-1 and SM21059-1 at MIRIAM beamline B22. Two anonymous reviewers provided constructive comments.

DATA ACCESSIBILITY

Synchrotron-based Fourier Transform Infrared microspectroscopy data collected at the Diamond Light Source and used to build figure 4 are available in the Supplementary Material.

FUNDING

This work was supported by All Souls College, Diamond Light Source (SM15975-1 and SM21059-1), Geological Society of America, Geological Society of London, NASA Astrobiology Institute (NNA13AA90A), Yale Institute for Biospheric Studies, and Yale Peabody Museum of Natural History. RPA was supported by All Souls College and NASA (NNX14AP10H). This work was performed in part at the Center for Nanoscale Systems (CNS), a member of the National Nanotechnology Coordinated Infrastructure Network (NNCI), which is

supported by the National Science Foundation under NSF award no. 1541959. CNS is part of Harvard University.

FIGURE CAPTIONS

Figure 1: Studied microfossils with elemental distributions. Light photomicrographs of fossils in thin section. Locations of extracted vertical sections shown by pink bars. SEM micrographs of extracted vertical sections and EDS maps showing carbon and aluminium distributions. Carbon comprises the microfossils which are surrounded by a concentration of aluminium. Secondary electron (SE) or backscatter electron (BSE) SEM images were utilised to minimise charging effects. Specimen details are listed in table 1. SEM and EDS operating conditions for each map/image are listed in Supplementary Material (table S1). Light and SEM images of the Svanbergfjellet *Germinosphaera* specimen/vertical section are given in Supplementary Material (Fig. S1).

Figure 2: SEM secondary electron (SE) micrograph of a focussed ion beam-milled vertical section of *Siphonophycus* from the Wynniatt Formation. Microfossil cross-section is surrounded by a halo of a platy mineral likely to be kaolinite. Courser crystals with planar interlocking boundaries (likely muscovite) and large quartz grains are also highlighted. SEM operating conditions are listed in Supplementary Material (table S1).

Figure 3: Representative synchrotron-based FTIR microspectra. Top: Representative total spectra showing an average of spectra numbers 188, 189, 190, 203, 204, 205, 218, 219, 220 from Lakhandha *Siphonophycus*. Both M-OH bands are present plus a broad silicate peak at $\sim 1000\text{ cm}^{-1}$

1
2
3 432 which is not resolved in sufficient detail to interpret its mineralogical components. Below are
4
5 433 representative spectra from the M-OH region for each vertical section plotted on the same
6
7
8 434 vertical scale. Characteristic bands at ~ 3620 , ~ 3652 , and $\sim 3694\text{ cm}^{-1}$ are recorded for the vertical
9
10 435 sections from Lakhanda and Svanbergfjellet, while a single broad band between ~ 3500 and
11
12 436 $\sim 3700\text{ cm}^{-1}$ is recorded for the vertical sections from Wynniatt. Representative spectra numbers:
13
14
15 437 Lakhanda *Siphonophycus* 237, Svanbergfjellet *Proterocladus* 150, *Germinosphaera* 150, and
16
17 438 microfossil fragment 263, and Wynniatt ?*Ostiana* 240 and *Siphonophycus* 204. See
18
19 439 Supplementary Material (table S2) for FTIR data spectra numbers.
20

21
22 440
23
24 441 Figure 4: Synchrotron-based FTIR microspectroscopy maps of compositional variation indicated
25
26 442 by the areas below the $\sim 3694\text{ cm}^{-1}$ band, the entire M-OH region (integrated band intensities in
27
28 443 arbitrary units), and the ratio of these two areas, for Lakhanda and Svanbergfjellet vertical
29
30
31 444 sections which show clearly defined M-OH bands. The light microscopy images of vertical
32
33 445 sections (left) indicate the position of the microfossils (red boxes). See text for further details.
34

35 446
36
37 447 Table 1: Interpreted phylogenetic affinities and associated biopolymers of the studied
38
39 448 microfossils: Lakhanda [24, 25], Svanbergfjellet [2, 26, 28, 70], Wynniatt [27]. Biopolymers
40
41
42 449 taken from [46-50].
43

44 450
45
46
47 451 Table 2: Bulk powder XRD Results. Percentage of each rock sample composed of different
48
49 452 minerals is calculated by the Reference Intensity Ratio Method [29]. Clay speciation is also
50
51 453 presented as a % of total clay (glauconite + illite 1 + illite 2 + kaolinite) using the relative areas
52
53
54 454 of weak but diagnostic peaks from 060/33-1 [30]. Qtz = quartz, Musc = muscovite, Chl =

chlorite, Kaol = kaolinite, Gl = glauconite, and Il1 and Il2 = two varieties of illite. Lakhanda sample LK62, Svanbergfjellet sample 99-L-15, Wynniatt sample 88-KL-131.

Figure S1: Left, light photomicrograph of Svanbergfjellet *Germinosphaera* specimen in thin section; pink bars show location of extracted vertical sections. Right, SEM backscatter electron (BSE) micrograph of extracted vertical section. SEM operating conditions are listed in Supplementary Material (table S1).

Figure S2: Selected EDS maps of vertical sections. Distributions of calcium, chlorine, iron, potassium, magnesium, oxygen, sulphur, and silicon are plotted. Pink bars on light photomicrographs of fossils in thin section show locations of extracted vertical sections. Scanning electron micrographs of extracted vertical sections are shown for reference. Secondary electron (SE) or backscatter electron (BSE) SEM images were utilised to minimise charging effects. SEM and EDS operating conditions for each map/image are listed in Supplementary Material (table S1).

Table S1: SEM and EDS operating conditions: accelerating voltages and detector types.

Table S2: Raw synchrotron-based FTIR microspectroscopy data.

REFERENCES

- [1] Knoll, A.H. 2003 *Life on a Young Planet: The first 3 billion years of evolution on earth*. Princeton, New Jersey, Princeton University Press.
- [2] Butterfield, N.J. 2015 Early evolution of the Eukaryota. *Palaeontology* **58**, 5-17. (doi:10.1111/pala.12139).

- [3] Butterfield, N.J. 2015 Proterozoic photosynthesis—a critical review. *Palaeontology* **58**, 953–972. (doi:10.1111/pala.12211).
- [4] Cohen, P.A. & Macdonald, F.A. 2015 The Proterozoic record of eukaryotes. *Paleobiology* **41**, 610–632. (doi:10.1017/pab.2015.25).
- [5] Knoll, A.H. 2014 Paleobiological perspectives on early eukaryotic evolution. *Cold Spring Harbor Perspectives in Biology* **6**. (doi:10.1101/cshperspect.a016121).
- [6] Muscente, A.D., Schiffbauer, J.D., Broce, J., Laflamme, M., O'Donnell, K., Boag, T.H., Meyer, M., Hawkins, A.D., Huntley, J.W., McNamara, M.E., et al. 2017 Exceptionally preserved fossil assemblages through geologic time and space. *Gondwana Research* **48**, 164–188. (doi:10.1016/j.gr.2017.04.020).
- [7] Butterfield, N.J. 1995 Secular distribution of Burgess-Shale-type preservation. *Lethaia* **28**, 1–13. (doi:10.1111/j.1502-3931.1995.tb01587.x).
- [8] Gaines, R.R. 2014 Burgess Shale-type preservation and its distribution in space and time. *Paleontological Society Papers* **20**, 123–146. (doi:10.1017/S1089332600002837).
- [9] Anderson, R.P., Tosca, N.J., Gaines, R.R., Mongiardino Koch, N. & Briggs, D.E.G. 2018 A mineralogical signature for Burgess Shale-type fossilization. *Geology* **46**, 347–350. (doi:10.1130/G39941.1).
- [10] Saleh, F., Pittet, B., Perrillat, J.-P. & Lefebvre, B. 2019 Orbital control on exceptional fossil preservation. *Geology* **47**, 103–106. (doi:10.1130/G45598.1).
- [11] McMahon, S., Anderson, R.P., Saupe, E.E. & Briggs, D.E.G. 2016 Experimental evidence that clay inhibits bacterial decomposers: Implications for preservation of organic fossils. *Geology* **44**, 867–870. (doi:10.1130/G38454.1).
- [12] Naimark, E., Kalinina, M., Shokurov, A., Boeva, N., Markov, A. & Zaytseva, L. 2016 Decaying in different clays: Implications for soft-tissue preservation. *Palaeontology* **59**, 583–595. (doi:10.1111/pala.12246).
- [13] Naimark, E.B., Kalinina, M.A., Shokurov, A.V., Markov, A.V. & Boeva, N.M. 2016 Decaying of *Artemia salina* in clay colloids: 14-month experimental formation of subfossils. *Journal of Paleontology* **90**, 472–484. (doi:10.1017/jpa.2016.23).
- [14] Wilson, L.A. & Butterfield, N.J. 2014 Sediment effects on the preservation of Burgess Shale-type compression fossils. *Palaaios* **29**, 145–154. (doi:10.2110/palo.2013.075).
- [15] Martin, D., Briggs, D.E.G. & John Parkes, R. 2003 Experimental mineralization of invertebrate eggs and the preservation of Neoproterozoic embryos. *Geology* **31**, 39–42. (doi:10.1130/0091-7613(2003)031<0039:EMOIEA>2.0.CO;2).
- [16] Naimark, E., Kalinina, M. & Boeva, N. 2018 Persistence of external anatomy of small crustaceans in a long term taphonomic experiment. *Palaaios* **33**, 154–163.

- [17] Naimark, E., Kalinina, M., Shokurov, A., Markov, A., Zaytseva, L. & Boeva, N. 2018 Mineral composition of host sediments influences the fossilization of soft tissues. *Can. J. Earth Sci.* **55**, 1271–1283. (doi:10.1139/cjes-2017-0237).
- [18] Newman, S., Daye, M., Fakra, S.C., Marcus, M.A., Pajusalu, M., Pruss, S.B., Smith, E.F. & Bosak, T. 2019 Experimental preservation of muscle tissue in quartz sand and kaolinite. *Palaios* **34**, 437–451. (doi:10.2110/palo.2019.030).
- [19] Orr, P.J., Briggs, D.E.G. & Kearns, S.L. 1998 Cambrian Burgess Shale animals replicated in clay minerals. *Science* **281**, 1173–1175. (doi:10.1126/science.281.5380.1173).
- [20] Anderson, R.P. 2019 Clay minerals and the fossilisation of early complex life. In *The origin and rise of complex life: integrating models, geochemical and palaeontological data* (eds. R. Wood, A.G. Liu, T.M. Lenton, S.W. Poulton & P.C.J. Donoghue). London, The Royal Society.
- [21] Anderson, E.P., Schiffbauer, J.D. & Xiao, S.H. 2011 Taphonomic study of Ediacaran organic-walled fossils confirms the importance of clay minerals and pyrite in Burgess Shale-type preservation. *Geology* **39**, 643–646. (doi:10.1130/G31969.1).
- [22] Wacey, D., Brasier, M.D., Parnell, J., Culwick, T., Bowden, S., Spinks, S., Boyce, A.J., Davidheiser-Kroll, B., Jeon, H., Saunders, M., et al. 2016 Contrasting microfossil preservation and lake chemistries within the 1200–1000 Ma Torridonian Supergroup of NW Scotland. In *Earth System Evolution and Early Life: A Celebration of the Work of Martin Brasier* (eds. A.T. Brasier, D. McIlroy & N. McLoughlin). London, Geological Society, London.
- [23] Wacey, D., Saunders, M., Roberts, M., Menon, S., Green, L., Kong, C., Culwick, T., Strother, P. & Brasier, M.D. 2014 Enhanced cellular preservation by clay minerals in 1 billion-year-old lakes. *Scientific Reports* **4**. (doi:10.1038/srep05841).
- [24] Hermann, T.N. & Podkovyrov, V.N. 2010 A discovery of Riphean heterotrophs in the Lakhanda Group of Siberia. *Paleontological Journal* **44**, 374–383. (doi:10.1016/j.precamres.2009.04.006).
- [25] Herman, T.N. 1990 *Organic world one billion years ago*. Leningrad, Nauka.
- [26] Butterfield, N.J., Knoll, A.H. & Swett, K. 1994 Paleobiology of the Neoproterozoic Svanbergfjellet Formation, Spitsbergen. *Fossils and Strata* **34**, 1–84. (doi:10.1111/j.1502-3931.1994.tb01558.x).
- [27] Butterfield, N.J. & Rainbird, R.H. 1998 Diverse organic-walled fossils, including "possible dinoflagellates," from the early Neoproterozoic of arctic Canada. *Geology* **26**, 963–966. (doi:10.1130/0091-7613(1998)026<0963:DOWFIP>2.3.CO;2).
- [28] Tang, Q., Pang, K., Yuan, X. & Xiao, S. 2020 A one-billion-year-old multicellular chlorophyte. *Nature Ecology and Evolution*. (doi:10.1038/s41559-020-1122-9).
- [29] Snyder, R.L. & Bish, D.L. 1989 Quantitative analysis. *Reviews in Mineralogy and Geochemistry* **20**, 101–144.

- [30] Środoń, J., Drits, V.A., McCarty, D.K., Hsieh, J.C.C. & Eberl, D.D. 2001 Quantitative X-Ray diffraction analysis of clay-bearing rocks from random preparations. *Clays and Clay Minerals* **49**, 514–528.
- [31] Russell, J.D. & Fraser, A.R. 1994 Infrared methods. In *Clay Mineralogy: Spectroscopic and Chemical Determinative Methods* (ed. M.J. Wilson), pp. 11–67. London, Chapman and Hall.
- [32] Thomson, D., Rainbird, R.H. & Dix, G. 2014 Architecture of a Neoproterozoic intracratonic carbonate ramp succession: Wynniatt Formation, Amundsen Basin, Arctic Canada. *Sedimentary Geology* **299**, 119–138. (doi:10.1016/j.sedgeo.2013.11.005).
- [33] Wilson, M.J. 2013 *Rock forming minerals, 3C: Clay minerals*. London, The Geological Society of London; 724 p.
- [34] Marshall, C.P., Javaux, E.J., Knoll, A.H. & Walter, M.R. 2005 Combined micr-Fourier transform infrared (FTIR) spectroscopy and micro-Raman spectroscopy of Proterozoic acritarchs: A new approach to Palaeobiology. *Precambrian Research* **138**, 208–224. (doi:10.1016/j.precamres.2005.05.006).
- [35] Podkovyrov, V.N. 2009 Mesoproterozoic Lakhanda Lagerstätte, Siberia: Paleoecology and taphonomy of the microbiota. *Precambrian Research* **173**, 146–153. (doi:10.1016/j.precamres.2009.04.006).
- [36] Powell, W. 2003 Greenschist-facies metamorphism of the Burgess Shale and its implications for models of fossil formation and preservation. *Can. J. Earth Sci.* **40**, 13–25. (doi:10.1139/e02-103).
- [37] Briggs, D.E.G. & Kear, A.J. 1993 Fossilization of soft tissue in the laboratory. *Science* **259**, 1439–1442. (doi:10.1126/science.259.5100.1439).
- [38] Skujinš, J., Pukite, A. & McLaren, A.D. 1974 Adsorption and activity of chitinase on kaolinite. *Soil Biology and Biochemistry* **6**. (doi:10.1016/00380717(74)90024-8).
- [39] Theng, B.K.G. 1974 *The chemistry of clay-organic reactions*. New York, John Wiley and Sons; 343 p.
- [40] Yu, W.H., Li, N., Tong, D.S., Zhou, C.H., Lin, C.X. & Xu, C.Y. 2013 Adsorption of proteins and nucleic acids on clay minerals and their interactions: A review. *Applied Clay Science* **80–81**, 443–452. (doi:10.1016/j.clay.2013.06.003).
- [41] Sposito, G. 1984 *The surface chemistry of soils*. Oxford, Oxford University Press; 234 p.
- [42] Liu, X., Lu, X., Sprik, M., Cheng, J., Meijer, E.J. & Wang, R. 2013 Acidity of edge surface sites of montmorillonite and kaolinite. *Geochimica et Cosmochimica Acta* **117**, 180–190. (doi:10.1016/j.gca.2013.04.008).

- [43] Solomon, D.H. & Rosser, M.J. 1965 Reactions catalyzed by minerals. Part 1. Polymerization of styrene. *Jouranal of Applied Polymer Science* **9**, 1261–1271. (doi:10.1002/app/1965.070090407).
- [44] Pan, C., Geng, A., Zhong, N. & Liu, J. 2010 Kerogen pyrolysis in the presence and absence of water and minerals: Steranes and triterpenoids. *Fuel* **89**, 336–345. (doi:10.1016/j.fuel.2009.06.032).
- [45] Stimler, N.P. & Tanzer, M.L. 1977 Location of the intermolecular cross linking sites in collagen. In *Protein crosslinking* (ed. M. Friedman), pp. 675–697. Boston, Springer.
- [46] Briggs, D.E.G. & Summons, R.E. 2014 Ancient biomolecules: Their origins, fossilization, and role in revealing the history of life. *Bio Essays* **36**, 482–490. (doi:10.1002/bies.201400010).
- [47] Tegelaar, E.W., de Leeuw, J.W., Derenne, S. & Largeau, C. 1989 A reappraisal of kerogen formation. *Geochimica et Cosmochimica Acta* **53**, 3103–3106. (doi:10.1016/0016-7037(89)90191-9).
- [48] Hoiczyk, E. 1998 Structural and biochemical analysis of the sheath of *Phormidium uncinatum*. *Journal of Bacteriology* **180**, 3923–3932.
- [49] Walsh, K., Jones, G.J. & Hugh Dunstan, R. 1997 Effect of irradiance on fatty acid, carotenoid, total protein composition and growth of *Microcystis aeruginosa*. *Photochemistry* **44**, 817–824. (doi:10.1016/S0031-9422(96)00573-0).
- [50] Bernard, S., Benzerara, K., Beyssac, O., Balan, E. & Brown Jr., G.E. 2015 Evolution of the macromolecular structure of sporopollenin during thermal degradation. *Heliyon*, e00034. (doi:10.1016/j.heliyon.2015.e00034).
- [51] Saleh, F., Antcliffe, J.B., Lefebvre, B., Pittet, B., Laibl, L., Perez, F., Lustri, L., Gueriau, P. & Daley, A.C. 2020 Taphonomic bias in exceptionally preserved biotas. *Earth and Planetary Science Letters* **529**, 115873. (doi:10.1016/j.epsl.2019.115873).
- [52] Konhauser, K.O., Fisher, Q.J., Fyfe, W.S., Longstaffe, F.J. & Powell, M.A. 1998 Authigenic mineralization and detrital clay binding by freshwater biofilms: The Brahmani river, India. *Geomicrobiology Journal* **15**, 209–222. (doi:10.1080/01490459809378077).
- [53] Konhauser, K.O., Fyfe, W.S., Ferris, F.G. & Beveridge, T.J. 1993 Metal sorption and mineral precipitation by bacteria in two Amazonian river systems: Rio Solimoes and Rio Negro, Brazil. *Geology* **161**, 399–413. (doi:10.1130/0091-7613(1993)021<1103:MSAMPB>2.3.CO;2).
- [54] Konhauser, K.O. & Urrutia, M.O. 1999 Bacterial clay authigenesis: a common biogeochemical process. *Chemical Geology* **161**, 399–413. (doi:10.1016/S0009-2541(99)00118-7).
- [55] Ferris, F.G., Fyfe, W.S. & Beveridge, T.J. 1988 Metallic ion binding by *Bacillus sibtills*: Implications for the fossilization of microorganisms. *Geology* **16**. (doi:10.1130/0091-7613(1988)016<0149:MIBBBS>2.3.CO;2).

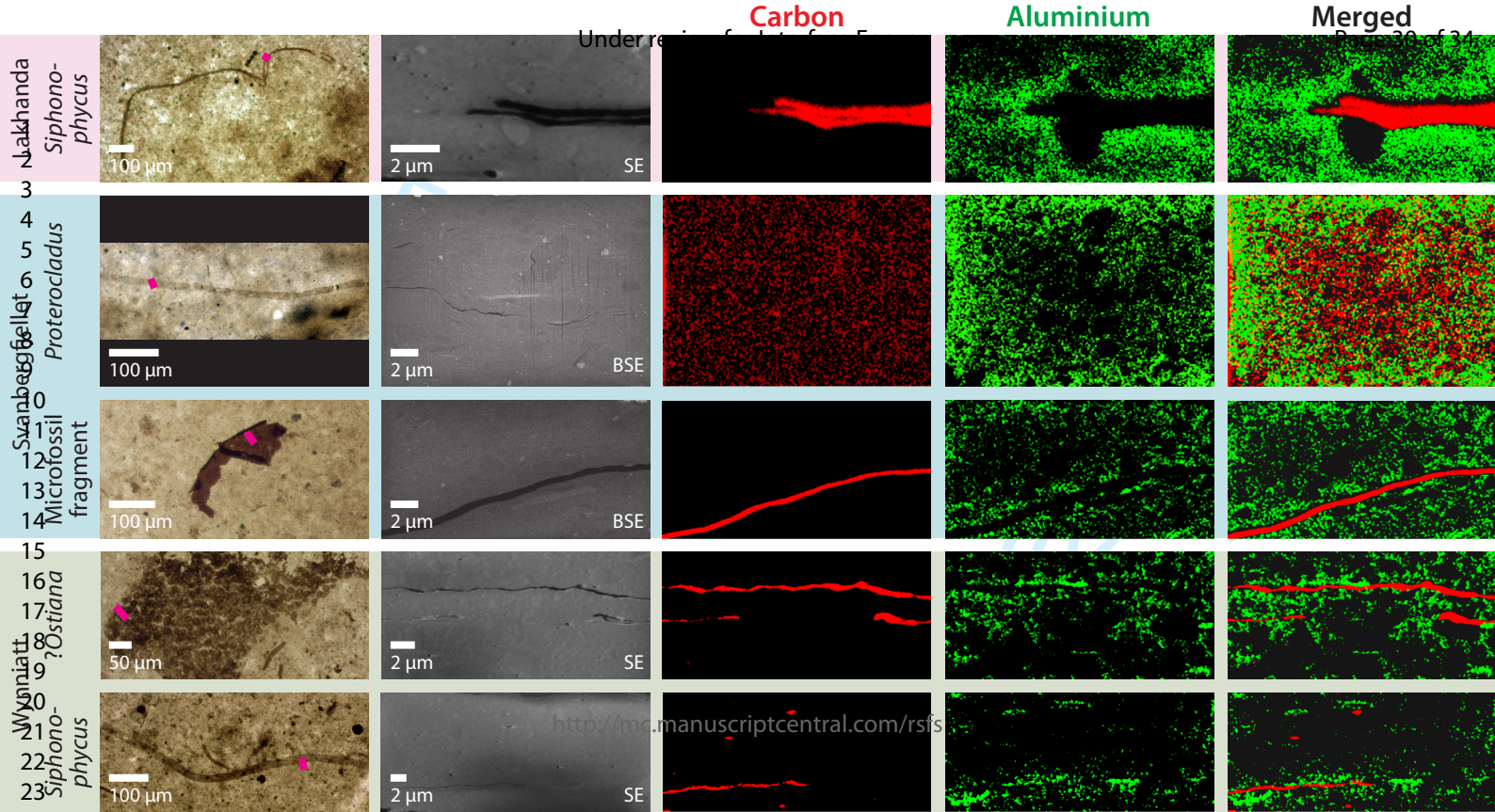
- [56] Newman, S.A., Klepac-Ceraj, V., Mariotti, G., Pruss, S.B., Watson, N. & Bosak, T. 2017 Experimental fossilization of mat-forming cyanobacteria in coarse-grained siliciclastic sediments. *Geobiology*, 1-15. (doi:10.1111/gbi.12229).
- [57] Newman, S.A., Mariotti, G., Pruss, S.B. & Bosak, T. 2016 Insights into cyanobacterial fossilization in Ediacaran siliciclastic environments. *Geology* **44**, 579–582. (doi:10.1130/G37791.1).
- [58] Knoll, A.H. 1985 Exceptional preservation of photosynthetic organisms in silicified carbonates and silicified peats. *Philosophical Transactions of the Royal Society B-Biological Sciences* **311**, 111-122. (doi:10.1098/rstb.1985.0143).
- [59] Li, Z.-X., Evans, D.A.D. & Halverson, G.P. 2013 Neoproterozoic glaciations in a revised global palaeogeography from the breakup of Rodinia to the assembly of Gondwanaland. *Sedimentary Geology* **294**, 219-232. (doi:10.1016/j.sedgeo.2013.05.016).
- [60] Halevy, I. & Bachan, A. 2017 The geologic history of seawater pH. *Science* **355**, 1069–1071. (doi:10.1126/science.aal4151).
- [61] dos Reis, M., Thawornwattana, Y., Angelis, K., Telford, M.J., Donoghue, P.C.J. & Yang, Z. 2015 Uncertainty in the timing of origin of animals and the limits of precision in molecular timescales. *Current Biology* **25**, 2939-2950. (doi:10.1016/j.cub.2015.09.066).
- [62] Bobrovskiy, I., Hope, J.M., Ivantsov, A., Nettersheim, B.J., Hallmann, C. & Brocks, J.J. 2018 Ancient steroids establish the Ediacaran fossil Dickinsonia as one of the earliest animals. *Science* **361**, 1246–1249. (doi:10.1126/science.aat7228).
- [63] Runnegar, B. 1982 The Cambrian explosion: Animals or fossils? *Journal of the Geological Society of Australia* **29**, 395–411. (doi:10.1080/00167618208729222).
- [64] Betts, H.C., Puttick, M.N., Clark, J.W., Williams, T.A., Donoghue, P.C.J. & Pisani, D. 2018 Integrated genomic and fossil evidence illuminates life's early evolution and eukaryote origin. *Nature Ecology and Evolution* **2**, 1556–1562. (doi:10.1038/s41559-018-0644-x).
- [65] Briggs, D.E.G., Erwin, D.H. & Collier, F.J. 1994 *Fossils of the Burgess Shale*. Washington, D. C., Smithsonian Institution Press; 238 p.
- [66] Hou, X., Siveter, D.J., Siveter, D.J., Aldridge, R.J., Cong, P., Gabbott, S.E., Ma, X., Purnell, M.A. & Williams, M. 2017 *The Cambrian Fossils of Chengjiang, China: The Flowering of Early Animal Life*. Second Edition ed. Oxford, John Wiley & Sons Ltd.; 316 p.
- [67] Butterfield, N.J. & Harvey, T.H.P. 2012 Small carbonaceous fossils (SCFs): A new measure of early Paleozoic paleobiology. *Geology* **40**, 71-74. (doi:10.1130/g32580.1).
- [68] Harvey, T.H.P. & Butterfield, N.J. 2017 Exceptionally preserved Cambrian loriciferans and the early animal invasion of the meiobenthos. *Nature Ecology and Evolution* **1**, 0022. (doi:10.1038/s41559-016-0022).

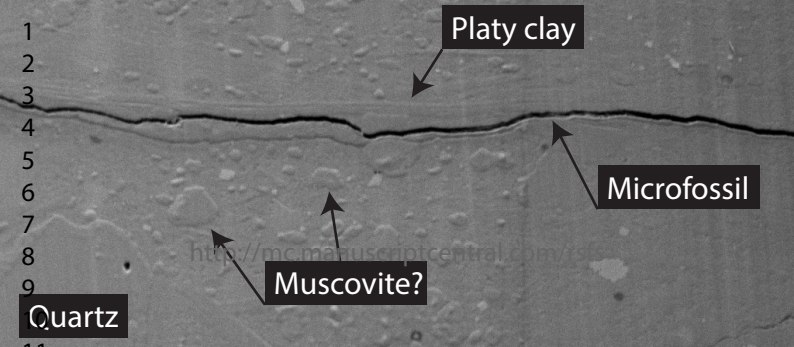
- [69] Butterfield, N.J. 2004 A vaucheriacean alga from the middle Neoproterozoic of Spitsbergen: implication for the evolution of Proterozoic eukaryotes and the Cambrian explosion. *Paleobiology* **30**, 231-252. (doi:10.1666/0094-8373(2004)030<0231:AVAFTM>2.0.CO;2).
- [70] Butterfield, N.J. 2005 Probable proterozoic fungi. *Paleobiology* **31**, 165-182. (doi:10.1666/0094-8373(2005)031<0165:ppf>2.0.co;2).
- [71] Butterfield, N.J. 2009 Modes of pre-Ediacaran multicellularity. *Precambrian Research* **173**, 201-211. (doi:10.1016/j.precamres.2009.01.008).
- [72] Cohen, P.A., Knoll, A.H. & Kodner, R.B. 2009 Large spinose microfossils in Ediacaran rocks as resting stages of early animals. *Proceedings of the National Academy of Sciences* **106**, 6519-6524. (doi:10.1073/pnas.0902322106).
- [73] Cornet, Y., François, C., Compère, P., Callec, Y., Roberty, S., Plumier, J.C. & Javaux, E.J. 2019 New insights on the palaeobiology, biostratigraphy, and paleogeography of the pre-Sturtian microfossil index taxon *Cerebrosphaera*. *Precambrian Research* **322**, 105410. (doi:10.1016/j.precamres.2019.105410).
- [74] Shang, X., Liu, P. & Moczyłowska, M. 2019 Acritarchs from the Doushantuo Formation at Liujing section in Songlin area of Guizhou Province, South China: Implications for early-middle Ediacaran biostratigraphy. *Precambrian Research* **334**, 105453. (doi:10.1016/j.precamres.2019.105453).
- [75] Tang, Q., Pang, T., Yuan, X. & Xiao, S. 2017 Electron microscopy reveals evidence for simple multicellularity in the Proterozoic fossil *Chuarina*. *Geology* **45**, 75–78. (doi:10.1130/G38680.1).
- [76] McMahon, S., Bosak, T., Grotzinger, J.P., Milliken, R.E., Summons, R.E., Newman, S., Fraeman, A., Williford, K.H. & Briggs, D.E.G. 2018 A field guide to finding fossils on Mars. *Journal of Geophysical Research: Planets* **123**, 1012–1040. (doi:10.1029/2017JE005478).
- [77] Ehlmann, B.L., Mustard, J.F., Murchie, S.L., Bibring, J.-P., Meunier, A., Fraeman, A.A. & Langevin, Y. 2011 Subsurface water and clay mineral formation during the early history of Mars. *Nature* **479**, 53–60. (doi:10.1038/nature10582).
- [78] Ehlmann, B.L., Mustard, J.F., Swayze, G.A., Clark, R.N., Bishop, J.L., Poulet, F., Des Marais, D.J., Roach, L.H., Milliken, R.E., Wray, J.J., et al. 2009 Identification of hydrated silicate minerals on Mars using MRO-CRISM: Geologic context near Nili Fossae and implications for aqueous alteration. *Journal of Geophysical Research: Planets* **114**, E00D08. (doi:10.1029/2009JE003339).
- [79] Cino, C.D., Dehouck, E. & McLennan, S.M. 2017 Geochemical constraints on the presence of clay minerals in the Burns formation, Meridiani Planum, Mars. *Icarus* **281**, 137–150. (doi:10.1016/j.icarus.2016.08.029).
- [80] Cuadros, J. 2015 Clays are messy—also on Mars. *American Mineralogist* **100**, 669–670. (doi:10.2138/am-2015-5229).

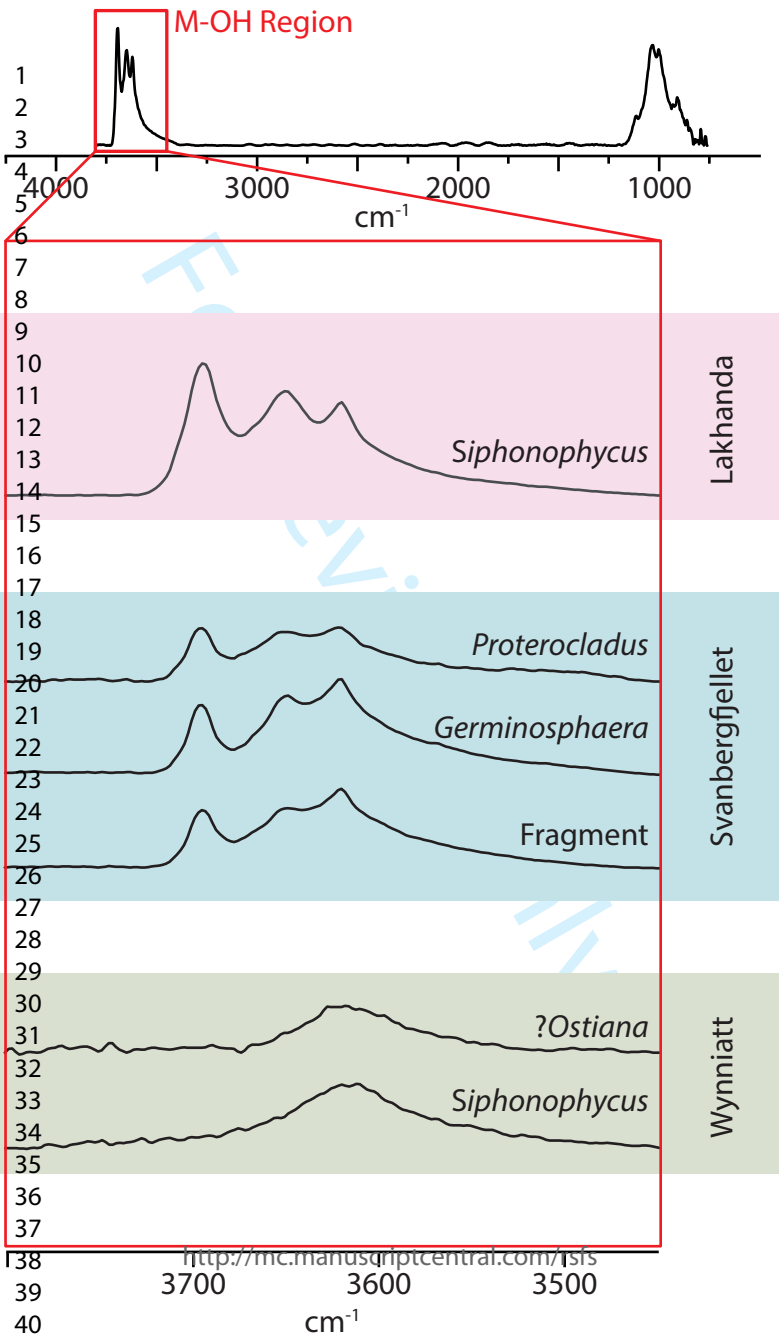
1
2
3
4
5
6
7
8
9
10
11
12
13
14
15
16
17
18
19
20
21
22
23
24
25
26
27
28
29
30
31
32
33
34
35
36
37
38
39
40
41
42
43
44
45
46
47
48
49
50
51
52
53
54
55
56
57
58
59
60

[81] Xiao, S., Yuan, X., Steiner, M. & Knoll, A.H. 2002 Macroscopic carbonaceous compressions in a terminal Proterozoic shale: A systematic reassessment of the Miaohu biota, South China. *Journal of Paleontology* **76**, 347–376. (doi:10.1666/0022-3360(2002)076<0347:MCCIAT>2.0.CO;2).

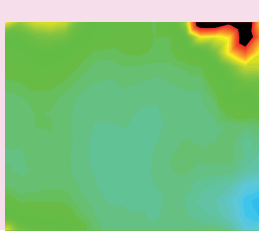
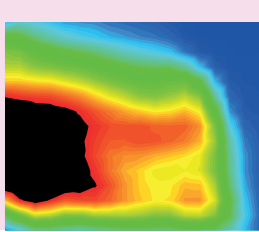
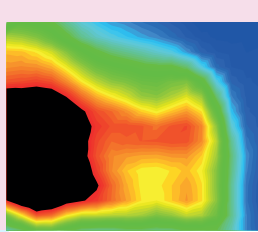
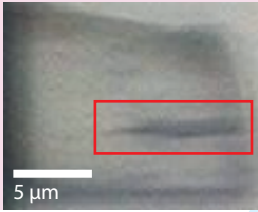
For Review Only



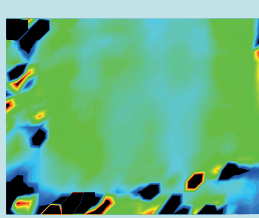
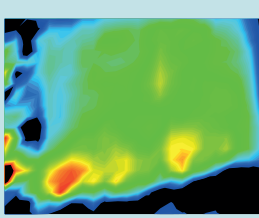
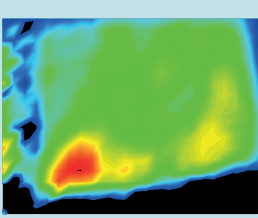
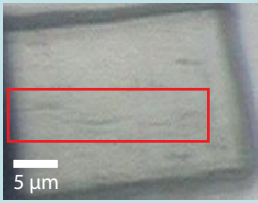




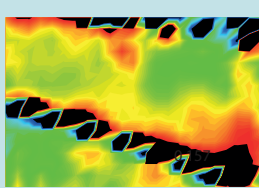
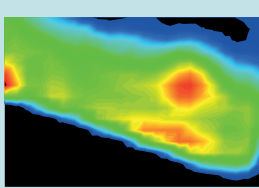
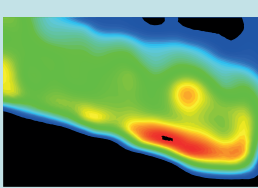
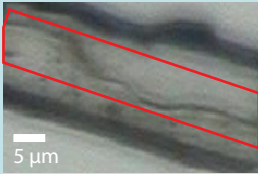
4 *Alshanda*
5 *Siphonophycus*
6



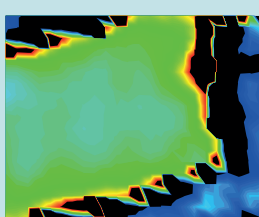
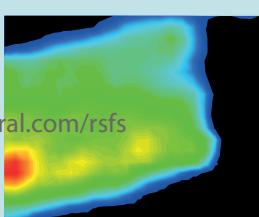
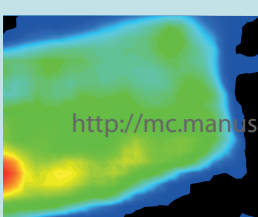
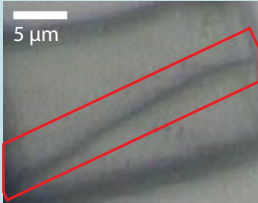
7
8 *Proterocladus*
9
10
11
12
13



14 *Svanbergella*
15 *Germinosphaera*
16
17
18
19
20



21
22
23
24
25
26
27



| | Phylogenetic affinity | Principal biopolymer | Thin-section, University collection, England finder coordinates |
|--|--|--|---|
| Lakhanda | | | |
| <i>Siphonophycus</i> | ?cyanobacterium | Sheaths of carbohydrate fibrils | LK62, Cambridge, N32/2 |
| Svanbergfjellet | | | |
| <i>Proterocladus major</i> | chlorophyte | Carbohydrates including cellulose | 86-G-62-52, Harvard, N47/2 |
| <i>Germinosphaera fibrilla</i> | ?eukaryote (possible vaucheriacean alga or fungus) | Likely aliphatic composition similar to sporopollenin or algaenan | 86-G-62-68, Harvard, Q48/4 |
| Microfossil fragment | ?eukaryote | Undetermined | 86-G-62-54, Harvard, L26/2 |
| Wynniatt | | | |
| ? <i>Ostiana</i> (or possibly <i>Palaeastrum</i>) | ?cyanobacterium (or ?chlorophyte) | Lipids and proteins with possible sheaths of carbohydrate fibrils (or, in the case of ?chlorophyte, carbohydrates including cellulose) | 88-KL-131-2, Cambridge, D35/2 |
| <i>Siphonophycus</i> | ?cyanobacteria | Sheaths of carbohydrate fibrils | 88-KL-131-2, Cambridge, Q46/2 |

1
2
3
4
5
6
7
8
9
10
11
12
13
14
15
16
17
18
19
20
21
22
23
24
25
26
27
28
29
30
31
32
33
34
35
36
37
38
39
40
41
42
43
44
45
46
47
48
49
50
51
52
53
54
55
56
57
58
59
60

| | Reference Intensity Ratio % | | | | 060/33-1 % Total Clay | | | |
|-----------------|-----------------------------|------|-----|------|-----------------------|-----|------|------|
| | Qtz | Musc | Chl | Kaol | Gl | Il1 | Il2 | Kaol |
| Lakhanda | 58 | 34 | 0 | 8 | 0 | 0 | 33.8 | 66.2 |
| Svanbergfjellet | 27 | 65 | 7 | 0 | 0 | 6.6 | 62.6 | 30.7 |
| Wynniatt | 26 | 74 | 0 | 0 | 10 | 90 | 0 | 0 |

For Review Only